Magnetic gates and guides for superconducting vortices

V. K. Vlasko-Vlasov, F. Colauto, Alexandre I. Buzdin, D. Rosenmann, T. Benseman, W.-K. Kwok

Magnetic gates and guides for superconducting vortices

V. K. Vlasko-Vlasov,[1] F. Colauto,[1,2] A. I. Buzdin,[3] D. Rosenmann,[1] T. Benseman,[1,4] and W.-K. Kwok[1]

[1]*Argonne National Laboratory, 9700 South Cass Avenue, Argonne, Illinois 60439, USA*

[2]*Departamento de Fisica, Universidade Federal de São Carlos, 13565-905, São Carlos, São Paulo, Brazil*

[3]*University Bordeaux, LOMA Centre national de la recherche scientifique (CNRS)–Unités mixtes de recherche (UMR) 5798, F-33405 Talence Cedex, France*

[4]*City University of New York (CUNY), Queens College, Queens, New York 11367, USA*

We image the motion of superconducting vortices in niobium film covered with a regular array of thin permalloy strips. By altering the magnetization orientation in the strips using a small in-plane magnetic field, we can tune the strength of interactions between vortices and the strip edges, enabling acceleration or retardation of the superconducting vortices in the sample and consequently introducing strong tunable anisotropy into the vortex dynamics. We discuss our observations in terms of the attraction/repulsion between point magnetic charges carried by vortices and lines of magnetic charges at the strip edges and derive analytical formulas for the vortex-magnetic strips coupling. Our approach demonstrates the analogy between the vortex motion regulated by the magnetic strip array and electric carrier flow in gated semiconducting devices. Scaling down the geometrical features of the proposed design may enable controlled manipulation of single vortices, paving the way for Abrikosov vortex microcircuits and memories.

I. INTRODUCTION

It is clearly recognized that power dissipation is a major issue in contemporary high density semiconductor microcircuits for computers and communication technologies. In this regard, superconducting (SC) single flux quantum devices [1–7] provide a route towards novel digital microelectronics. Such cryodevices, based on SC elements with minute losses, offer superior performance in speed and exceptionally low power consumption. They operate with magnetic vortices, each carrying a single magnetic flux quantum [8] that can perform as natural bits for digital operations. The notion of utilizing SC vortices in digital microprocessors and memories has been discussed for a while (see references in Refs. [1–7]). However, presently their technical realization is still in the research and development stage. Most of the efforts in vortex technology, termed *fluxtronics*, are devoted to the design and study of Josephson vortex circuits, where single flux quantum functionality is achieved by fine tuning assemblies of Josephson junctions (see, e.g., Ref. [5]). Meanwhile, the alternative of constructing circuits based on single Abrikosov vortices remains largely unexplored. The idea of such devices was first suggested in the 1980s [9–14] and was revisited recently by the Stockholm group [7]. A number of proposed fluxonic devices relied on tunable trapping and translation of vortices in SC films with arrays of nanoholes of different shapes and symmetries [15–33]. Extensive citations on the subject can be found in Ref. [34]. These studies showed that it is possible to strongly enhance vortex pinning at integer and fractional matching fields, to induce guided motion of vortices, to realize vortex ratcheting or diode effects, and to synchronize vortex dynamics in ac fields.

Some of these works used small magnetic dots or ferromagnetic (FM) layers with domains in close proximity to a SC film to manipulate the SC transition temperature, T_c, and vortex dynamics. The micro- and nanopatterning of the FM layer allowed various designs where SC channels can exist between normal regions, in which T_c was suppressed by the stray fields of the FM structures. For example, it was possible to create SC channels along domain walls between normal state regions formed under FM domains (so-called domain wall superconductivity [35,36]) and subsequently to expand these channels by countering the stray fields' effect in the FM domains with an external field. Furthermore, guided vortex motion can be generated [30,37] with arrays of in-plane polarized magnetic nanobars, where the stray fields emanating from their ends produce weak channels of suppressed order parameter in the SC layer. Alternatively, magnetic arrays can provide strong, temperature independent magnetic pinning of vortices. For example, FM dots with perpendicular magnetic moments, **M**, can act as dipoles**,** attracting vortices polarized along the same direction towards their center while positioning oppositely polarized vortices at the dot's periphery, where the stray fields are aligned against **M**. For in-plane magnetized FM dots, there will be a dipolar potential with attraction and repulsion maxima for vortices located on opposite sides of the dot in the direction of **M**. Arrays of asymmetric magnetic dots (e.g., triangular) will form asymmetric potentials and thus assist unidirectional vortex motion along the asymmetry axis [18].

Early investigations of periodically patterned superconducting films and hybrid FM/SC structures were pioneered by the groups of Pannetier [38,39], Bruynseraede and Moshchalkov [40,41], Schuller and Vicent [42–44], and theoretically supported by works of Lyuksyutov and Pokrovky [45–47], Peeters and Milosevic [48–52], Nori, Reichhardt and Olson [15–17,20,53–55], and Carneiro [56–61] with collaborators. Together with more recent works, these studies demonstrated the high potential for vortex manipulation with magnetic structures. A broad analysis of the vortex dynamics in FM/SC hybrids is presented in a number of comprehensive reviews [62–64], describing the basic effects and the underlying physics. References to the latest works on the subject can be found in Refs. [65–69].

Our group also contributed to the studies of different hybrid structures, including bilayers of SC/FM films containing magnetic strip domains [70–73] and lithographically patterned FM strips with in-plane magnetization on top of a SC film [74]. We showed that FM stripe domains and the edges of FM strips could be used to guide vortices along them and serve as barriers for vortex motion across them. In our recent paper [75], we demonstrated that an array of *closely spaced* soft magnetic strips could allow triodelike control of Abrikosov vortices. By rotating the magnetization **M** of the strips using relatively small in-plane fields, the magnetic charge responsible for the stray fields at the strip edges can be easily tailored from zero (at **M**‖edge) to a maximum (at **M**⊥edge). Consequently, the strip edges can become easy channels or barriers for vortex motion. The strength of the barrier and flux channeling effects are both defined by the orientation of **M** with respect to the strip edges and by the magnitude of |**M**|. In this paper, we extend our work to samples with *larger interstrip* gaps, which allows us to reveal flux distributions at oppositely polarized strip edges and to image and analyze fine details of the vortex dynamics. We show that the main guidance and pinning effects occur at strip edges with the same magnetic charge polarity as that of entering vortices generated by an applied normal field, while the effect of oppositely charged edges is very weak.

II. EXPERIMENT AND DISCUSSION

A. Sample preparation

The sample is a $2 \times 2\,\mathrm{mm}^2$ square of 100 nm SC Nb film ($T_c = 8.7$ K) with parallel FM permalloy (Py) strips deposited on top. Both Nb and Py films were sputtered using a high-vacuum dc magnetron system. The Nb square was defined on oxidized Si substrate by laser lithography and, after sputtering and lift-off, covered with 15 nm SiO_2 layer to avoid proximity effects. Subsequently, an array of 35 μm wide and 40 nm thick Py strips with 5 μm gaps was fabricated on top of the Nb square, 200 μm away from the square edges using e-beam lithography and a lift-off process. An optical image of the sample is shown in Fig. 1(a).

The sample was covered with a garnet indicator film and placed on the cold finger of a closed cycle optical cryostat (Montana Instruments). Observations of the normal flux patterns at temperatures, T, ranging from 3.5 to 8.5 K were performed with a polarized light microscope using a magneto-optical (MO) imaging technique [76]. The sample was cooled to a fixed $T < T_c$ in the presence of a relatively small (20–150 Oe) in-plane field $H_{||}$, oriented at different angles with respect to the strips in order to polarize the Py strips. In the described experiments $H_{||}$ remained unchanged after cooling, securing the strip polarization. We checked that in-plane fields up to 1 kOe do not modify the normal flux dynamics in the reference 100 nm Nb film [77]. Background images revealing the stray fields at the edges of the Py strips, which depend on the strip polarization, were taken before application of the normal (perpendicular to the Nb film surface) field H_z. These images were then subtracted from the images taken with the applied normal field such that only new vortices generated by H_z would be displayed. Below, we illustrate the main features of the dynamics of the entering H_z vortices in the presence of transversely ($H_{||}$ along the strip width), longitudinally ($H_{||}$ along the strip length), and diagonally ($H_{||}$ at 45° to the strip pattern) polarized Py strips.

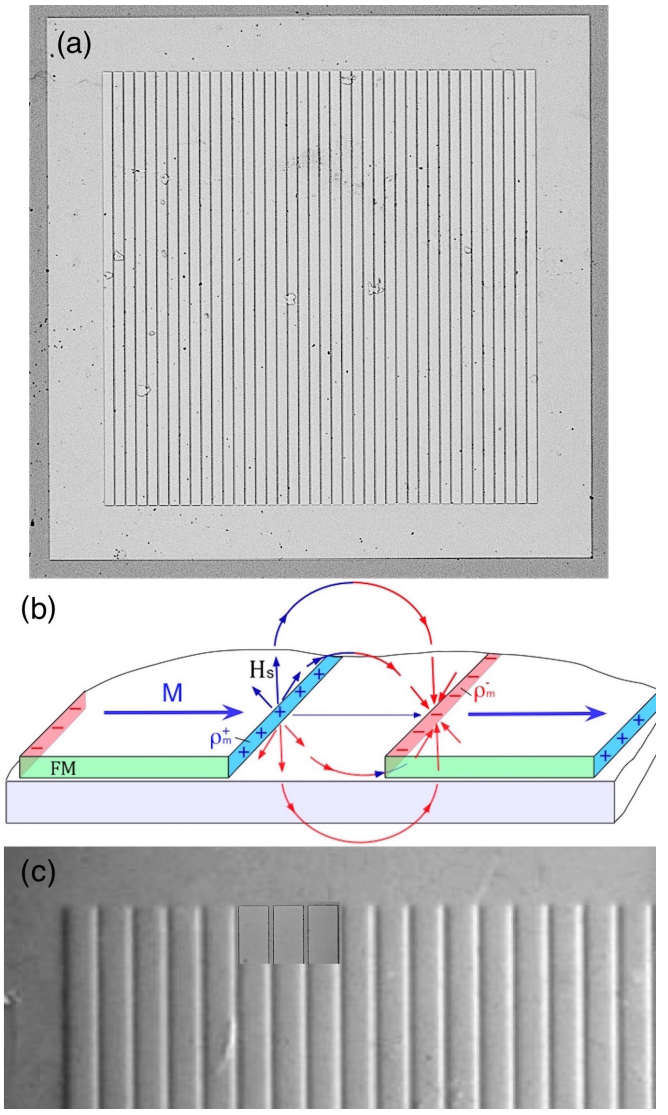

FIG. 1. (a) Optical picture of 2 × 2 mm Nb square with Py strips in the middle. (b) Schematic of magnetic charges along the long edges of transversely polarized Py strips. Each edge forms a magnetic monopole line with radially diverging magnetic stray fields H_s. (c) MO image of the stray fields induced by the array of transversely polarized Py strips. Bright and dark contrast indicate the up and down directions of H_s. The overlayed rectangle in (c) shows the positions of the strip ends and gaps.

B. Transverse polarization of Py strips

Our thin Py strips have the preferred magnetization direction in the film plane, negligible in-plane anisotropy, and a small coercivity. When an in-plane magnetic field of a few tens of Oersted is applied across the strips, their magnetic moments **M** orient parallel with the field and form strongly localized magnetic charges along the long edges of the strips [Fig. 1(b)]. The magnetic charge density is defined by the divergence of the magnetization near the strip edge, $\rho_M = -\mathrm{div}\mathbf{M}$. For strips

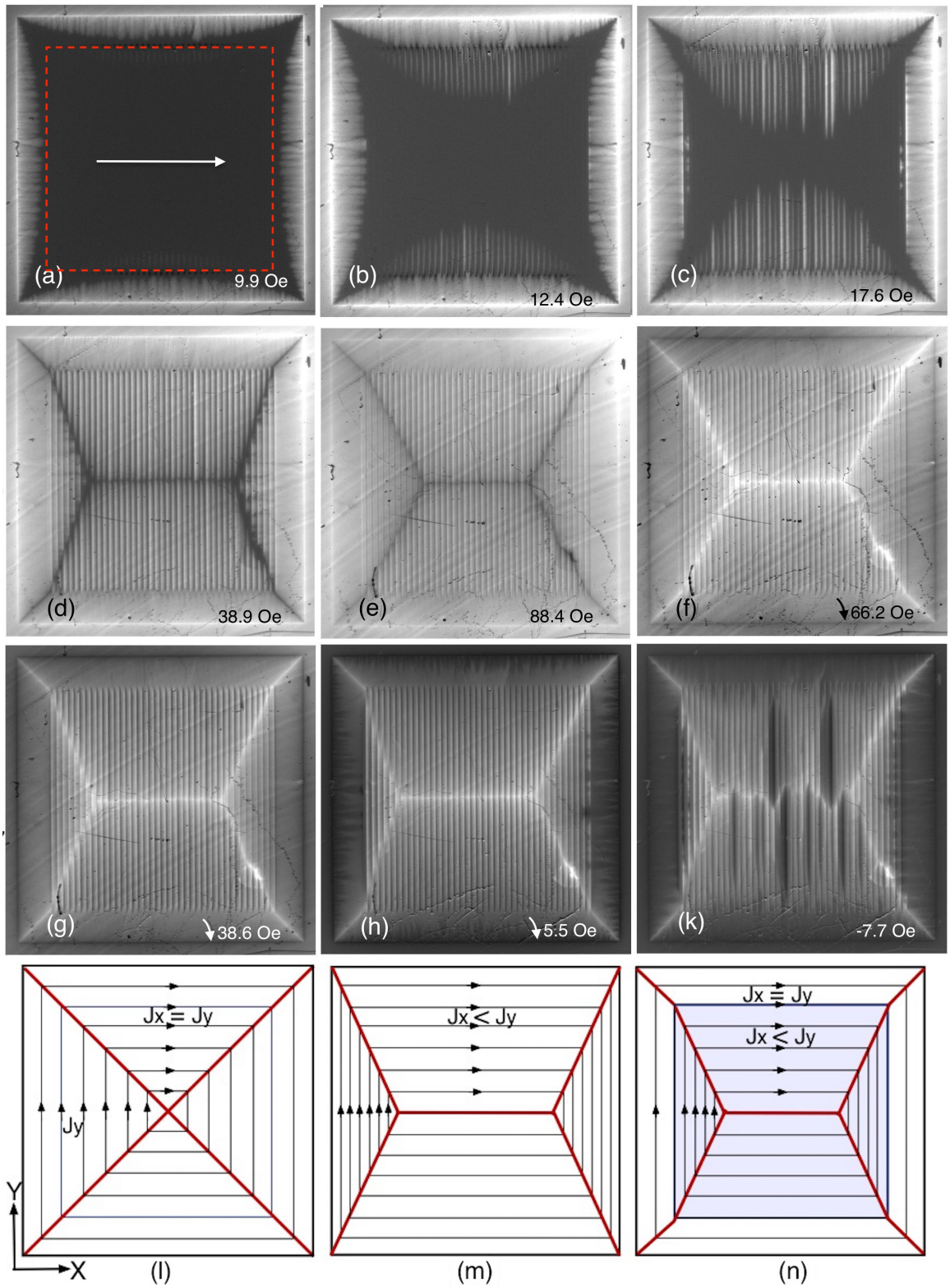

FIG. 2. MO images of the normal flux distribution in the sample with transversely polarized strips; $T = 4$ K. Direction of $H_{||}$ is shown by the arrow in (a). Dashed square in (a) outlines the area of the Py pattern. The applied normal field H_z increases in (a)–(e), decreases in (f)–(h), and changes sign in (k). Values of H_z are shown on the panels. Intensity of bright contrast corresponds to the density of positive H_z vortices. Dark contrast at the sample edges in (h)–(k) and along the strips in (k) reveals negative B_z. Current schemes at the bottom correspond to isotropic (l) and anisotropic (m) homogeneous samples and the sample with anisotropic middle part (n). In the presented geometrical model of the critical state (l)–(n) distances between the supercurrent lines are inversely proportional to the current density. The angle of the SCT lines, where maximum screening occurs in the increasing H_z [dark lines in (d) and (e)] or maximum trapped flux remains in the decreasing H_z [bright lines in (f)–(h)], is defined by the ratio of J_x/J_y.

with a rectangular cross section, ρ_M is proportional to the magnetization component M_n perpendicular to the edge face yielding surface charge density $\sigma_M = M_n$. Since the Py strip thickness, $d_f = 40\,\text{nm}$, is much smaller than the strip and gap width ($W = 35\,\mu\text{m}$ and $G = 5\,\mu\text{m}$, respectively), we can consider each strip edge as a magnetically charged filament with a linear charge density $M_n d_f$. The interaction of this linear charged edge with Abrikosov vortices, which can be described as point monopoles carrying magnetic charges of two flux quanta [78] $2\Phi_0$ [79], is analogous to the interaction between an electrically charged line and electric point charges. This analogy allows a straightforward intuitive analysis of the vortex behavior in our hybrid structure, as described below.

The magnetic charges produce alternating magnetic stray fields, H_s, at the Py strip edges, as revealed in Fig. 1(c) by the bright and dark contrast in the MO image. The dark and bright contrasts depict down and up directions of H_s, respectively, and correspond to the sign of the magnetic charge at each strip edge. In the following illustrations, these H_s generated MO patterns will be subtracted from images obtained with an additional *applied* normal-to-surface field, H_z, to reveal only vortex evolution generated by this field.

Small *normal* fields applied to thin SC films and plates are screened by a Meissner current, which induces concentrated H_z fields at the perimeter of our square Nb film visualized as bright contrast along the rim of the sample. With increasing H_z, Abrikosov vortices enter the film from all four sides of the sample in the shape of light flux lobes caused by defects and fractal flux dynamics (see Ref. [80] and references therein) in conditions of strongly nonlinear supercurrent flow [81]. They overlap and form a pillow-shaped flux front, as shown in Fig. 2(a). At larger H_z, the flux front advances inside the sample, arrives at the edges of the Py strips, and starts moving with different rates along and across the strips, resulting in an anisotropic pattern [shown in Figs. 2(b) and 2(c)]. Namely, the vortices enter with a noticeable delay *perpendicular* to the long edges of the Py strips and accumulate at the strip edges, forming bright lines of increased B_z along them near the left and right sides of the Py pattern [Fig. 2(c)]. Meanwhile, vortices easily enter and move deep inside the sample *along* the interstrip gaps, forming bright enhanced B_z lines clearly resolved near the top and bottom sides of the Py pattern in Figs. 2(b) and 2(c). With increasing H_z, the normal flux expands from the interstrip gap region into the area beneath the Py strips forming a modulated critical state. The B_z flux fronts propagating along the Py strips from the top and bottom sides meet at the horizontal center line of the sample, while the slower flux fronts advancing from the left and right sides remain far from the center of the sample. The resulting global critical state, when vortices occupy the whole sample, is shown in Fig. 2(d). The lines of dark contrast in Figs. 2(d) and 2(e) depict loci of the maximum screening of H_z corresponding to sharp turns of the supercurrent trajectories [see schemes in Figs. 2(l)–2(n)]. Angles of these sharp current turn (SCT) lines are defined by the anisotropy of the average critical currents (J_c) in appropriate areas. In the peripheral area devoid of the Py strips (within 200 μm from the Nb film edges), the SCT lines travel along the diagonals of the square. However, in the area under the Py strip pattern, the SCT lines are angled to reflect the enhanced average current *along* the strips, $J_c^{\parallel}$, and

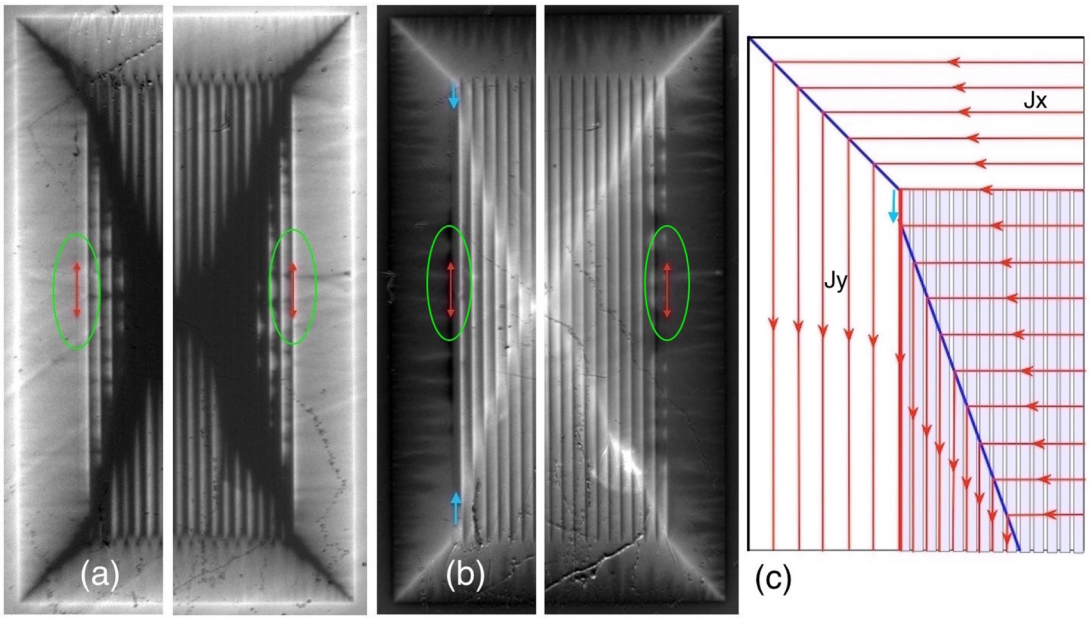

FIG. 3. Left-right asymmetry of the vortex patterns for transversely polarized Py strips. The left and right sides of the sample at 4 K in increasing [(a): $H_z = 23.8\,\text{Oe}$)] and decreasing field [(b): $H_z = 0$ after $H_z^{\max} = 276\,\text{Oe}$]. The furthest most left and right edges of the Py magnetic strips are marked by red double arrows. The shift of the bright SCT lines on the left side in (b) is shown by blue arrows. Positive vortices (bright) are not pinned at the most left strip edge in (a) (see left ellipse), but negative vortices (dark) are impeded at this edge in (b). Vice versa, positive vortices are delayed and accumulated at the most right edge in (a) (right ellipse), but negative vortices move across it smoothly in (b). (c) Schematic explaining the zigzag shift of the SCT line in (b) due to enhanced J_c along the left side of the magnetic pattern. Similar but smaller zigzag shifts appear at each interstrip gap [not shown on the schematic but revealed on zigzagging SCT lines in (b)].

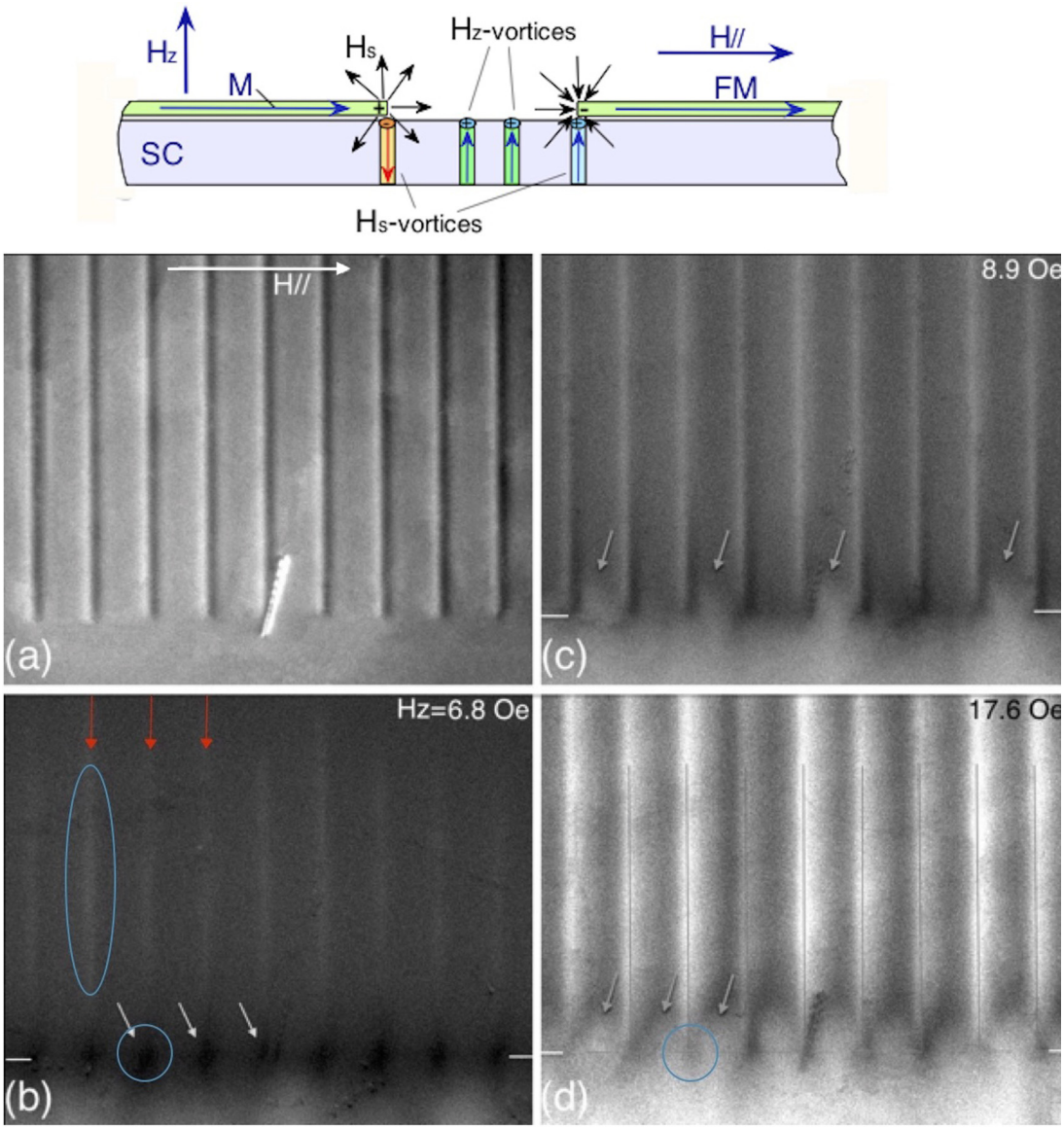

FIG. 4. Expanded view of the normal flux entry at small H_z near bottom ends of the strips. Schematic of stray fields H_s (top) and bright/dark contrast in (a) show up and down components of H_s due to the transversely polarized Py strips at $H_z = 0$. This contrast is subtracted from other MO images to reveal entering H_z vortices. $T = 5$ K; field values are shown on the panels. Short horizontal lines in (b)–(d) mark the position of strip ends. Tilted arrows in (b) (one encircled) mark dark spots of negative B_z due to the downward motion of negative H_s vortices. Brighter contrast along the strip edges in (b)–(d) reveals the advanced guided motion of the positive Abrikosov vortices [marked by vertical arrows and by ellipse in (b)]. Arrows in (c) and (d) point to the fingers of the secondary positive B_z front entering across the strip ends. Thin vertical lines in (d) mark the middle of the interstrip gaps. Circle in (d) marks the lower B_z spot near the strip corners.

reduced critical currents *across* the strips, $J_c^{\perp}$. An estimate of the anisotropy ratio from Fig. 2(d) yields $J_c^{\parallel}/J_c^{\perp} \sim 2.6$. When H_z is increased further, the MO picture remains qualitatively the same, although the anisotropy decreases, as demonstrated by the shortening of the dark central horizontal line in the critical state envelope in Fig. 2(e) ($J_c^{\parallel}/J_c^{\perp} \sim 1.9$). At an even larger normal field, the anisotropy reduces only slightly from this value.

Ramping the field down from a maximum (in this case, $H_z^{\max} = 276$ Oe) inverts the critical currents and the dark MO lines, corresponding to maximum screening transform into bright lines of maximum trapped B_z [Fig. 2(f)]. The envelopelike shape of the critical state pattern remains the same, as in the case for increasing H_z. With further decreasing field, the horizontal center line of the envelope lengthens, indicating the increased anisotropy of the critical currents at smaller B_z [Fig. 2(g)]. The decrease and increase of the anisotropy upon ramping the field up and down, respectively, demonstrate the competition of intervortex interactions with the effect of the magnetic strips.

Reducing H_z further causes negative flux (dark contrast) induced by the reversed currents to enter near the sample edges, and the critical state envelope shows a pronounced asymmetry with respect to the left and right sides of the strip array [Fig. 2(h)]. The horizontal center line shifts to the left, and the bright SCT lines on the left side of the Py

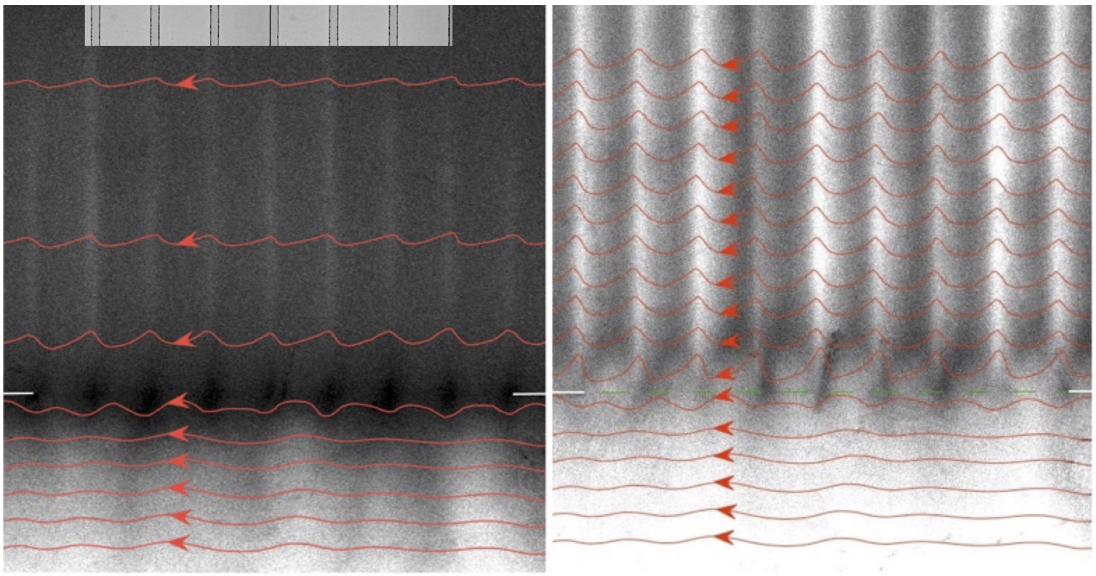

FIG. 5. Current trajectories (red lines) for the flux patterns in Figs. 4(b) and 4(d). Inset top left shows position of the strip gaps.

pattern become shorter. Also, a qualitative difference in the negative vortex entry is observed at the left and right sides of the sample. The asymmetry is better seen in the expanded view of the two sides upon both increasing and decreasing H_z in Fig. 3. With increasing H_z [Fig. 3(a)], the positive vortices are delayed at the first positively charged edge on the right but pass easier across the furthest most left negatively charged edge and accumulate at the next positive edge (the left and right edges of the Py pattern are marked by double arrows in Fig. 3). Hence, positively charged strip edges provide stronger pinning for positive H_z vortices than negatively charged edges. Such a behavior is unusual because the maximum pinning force, F_p, for the oppositely charged edges should be practically the same. We associate the asymmetry with the dynamic nature of the vortex crossing over the strip edges. When the positive vortex approaches the negatively charged line, it is attracted and accelerates towards the line. In contrast, a similar vortex approaching the positively charged line will decelerate and stop at the line.

With reducing H_z [Fig. 3(b)], the normal induction drops and changes sign around the most left edge of the Py pattern (contrast changes to dark), resulting in the increased local current along this edge. This yields a zigzag shift of the SCT line in the patterned area, as marked by the blue arrows in Fig. 3(b) and schematically shown in Fig. 3(c). The average direction of the SCT lines under the strips remains the same, but the triangular region bound by these lines on the left becomes smaller than that on the right. As a result, the centerline of the critical state envelope pattern extends to the left. At larger H_z, the left-right asymmetry disappears due to the increased vortex-vortex interactions overcoming the magnetic pinning. For opposite polarity of the transverse in-plane field, the asymmetric patterns mirror-flip horizontally.

Reducing the positive H_z field to zero and applying a negative H_z lead to advanced penetration of negative vortices along the Py strips [Fig. 2(k)], which eventually results in an anisotropic critical state similar to that in positive H_z (not shown). A new feature that emerges with increasing negative field is the unexpected appearance of extended negative vortex regions near the middle of the sample [dark streaks around the center line in Fig. 2(k)] prior to their formation near the top and bottom strip ends. These regions aligned with the strips appear irregularly across the horizontal SCT line. We associate them with dynamic instabilities caused by the strip-induced anisotropy of the vortex motion, which breaks the continuous loops of current flowing around the horizontal center line of the sample. As a result, a chain of current loops appear, supporting locally enhanced negative fields between them. The situation is similar to the inversion of field between current rings of the

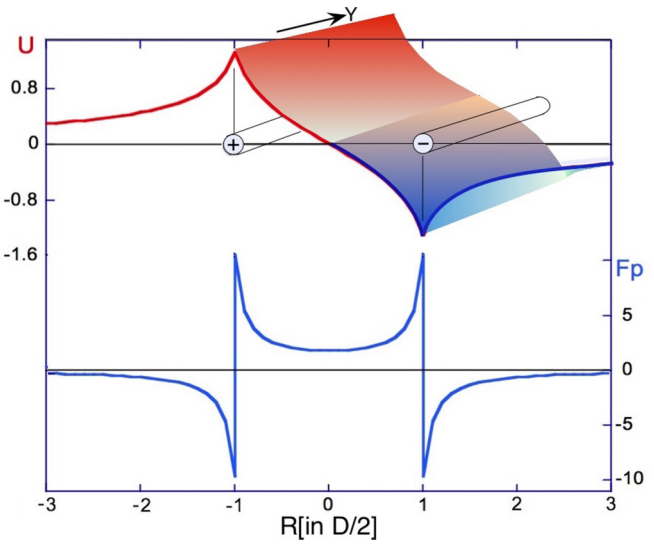

FIG. 6. The magnetic potential $U \sim \ln R$ (top) and magnetic pinning force $F_p \sim 1/R$ (bottom) for Abrikosov vortices moving across the gap between thin long transversely polarized FM strips. U and F_p are in arbitrary units, and the distance R is in units of half the gap (D/2) between the strips. Potential barrier ridge and potential valley groove are formed along positively and negatively charged edges respectively ($\|Y$).

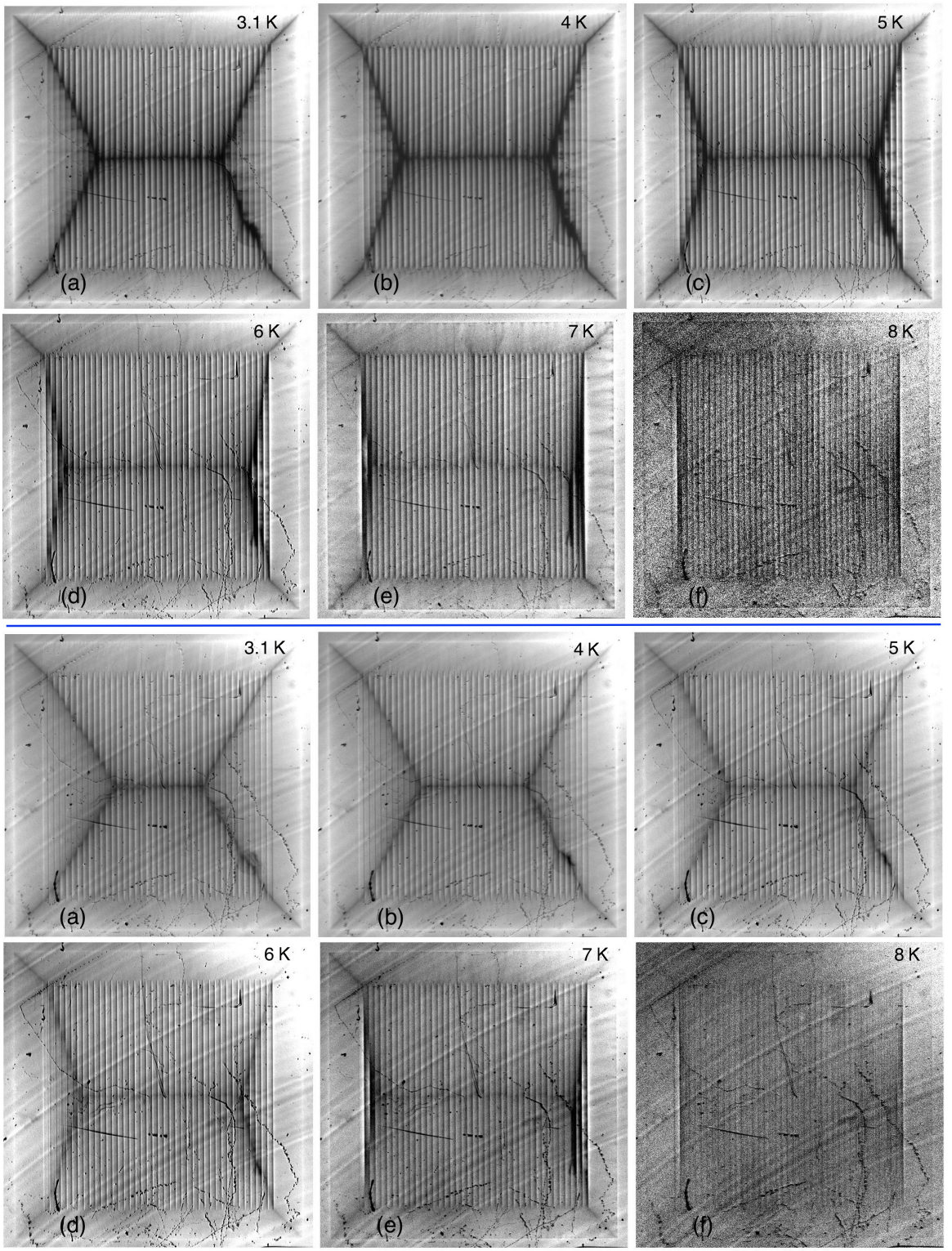

FIG. 7. Temperature variations of anisotropic critical states for transversely polarized strips at smaller field $H_{\rm fill}$, when vortices first fill the entire sample (top set: $H_{\rm fill}$ decreases from 55 Oe to 5 Oe with increasing T from 3.1 K to 8 K) and at larger field (bottom set: $H_z = 110$ Oe). The anisotropy increases with T and drops with H_z.

same chirality. At larger negative fields, these negative vortex regions merge, with streaks of negative B_z extending along the interstrip gaps from the top and bottom sides of the Py pattern, and form a structure similar to that observed with positive H_z. After ramping down the negative H_z, the positive vortices induced near the sample edges by the inverted critical currents are delayed stronger on the right side of the Py pattern but easily cross the leftmost strip. Also, the SCT center line shifts to the right. The asymmetry is opposite to that observed for negative vortex entry when reducing positive H_z.

Fine details of vortex entry dynamics induced by transversely polarized Py strips can be better seen in the MO images taken at larger magnification. Before the flux front induced by H_z reaches the tips of the Py strips, brighter lines of positive B_z appear along the longitudinal strip edges [marked by red vertical arrows and ellipse in Fig. 4(b)]. At the same time, dark spots of negative B_z emerge near the strip ends [marked by tilted arrows and circle in Fig. 4(b)]. This unusual behavior is associated with vortices formed upon cooling the sample through T_c in the presence of stray fields (H_s) at the long Py strip edges. As shown in the cross-section schematic of the sample in Fig. 4, near the longitudinal Py edges with positive magnetic charge and diverging stray field H_s, the H_s-created vortices carry negative B_z. At the opposing longitudinal edge of the adjacent Py strip with negative magnetic charge, the H_s vortices carry positive B_z. When an external H_z is ramped up at $T < T_c$, the Meissner current induced Lorentz force F_L acts on the H_s vortices in opposite directions. For positive H_s vortices, F_L is pointing inside the sample while for negative H_s vortices, F_L is directed towards the sample edges. When the B_z front approaches the ends of the strips, the Meissner current, J_M, ahead of the flux front becomes comparable with the critical current J_c flowing behind the front, and F_L overcomes the pinning force. As a consequence, the positive H_s vortices advance inside, while negative H_s vortices move to the ends of the strips where they assemble into dark droplets of negative B_z, as illustrated in Fig. 4(b). With further increasing field, incoming positive H_z-induced vortices annihilate these droplets and move into the interstrip gaps forming bright lines of enhanced positive B_z along them [Fig. 4(c)]. Also, the sharp B_z front enters in the shape of fingers across the uncharged ends of the Py strips [indicated by arrows in Fig. 4(c)]. At higher fields, the modulated B_z front advances inside the sample and forms an inhomogeneous distribution of B_z, where the density of vortices is maximum near the left sides of the gaps and smoothly decreases to the right [strips of bright contrast in Fig. 4(d)]. Thin lines in Fig. 4(d) mark the middle of the interstrip gaps. Clearly, new positive H_z vortices pile up on the left of the interstrip gaps at the positively charged strip edges, but they pass more easily to the right across neighboring negatively charged strip edges. This forms a flux gradient with B_z decaying rightward from the gap into the strips. The above flux pattern corresponds to the wiggling current trajectories sharply bending near the positively charged edge of the Py strips, as sketched in Fig. 5 [82]. Here the increasing B_z corresponds to the downward arching and decreasing B_z to the upward arching of the current lines, and sharper bends in the current trajectory yield enhanced concentration of positive vortices at the positive edges. In Fig. 5(a), the increasing distance between the current lines towards the top of the picture reflects the decay of the Meissner current towards the center of the sample. The meandering current trajectories yield spatially oscillating anisotropic supercurrent density. The longitudinal current density ($J_\parallel$ parallel to strips) is maximum, and the transverse current density ($J_\perp$ perpendicular to strips) is minimum at the positively charged strip edges. Towards the middle of the strips, $J_\parallel$ drops, and $J_\perp$ increases. The resulting SCT lines in the global critical state also meander but straighten with increasing H_z.

The described flux evolution, in the presence of the transversely polarized Py strips, is a consequence of the interactions between entering H_z vortices induced by the applied normal field and the magnetic potential formed at the edges of the strips. In the beginning these interactions are modified by the presence of field cooled H_s vortices. As already mentioned, we can consider edges of the thin Py strips polarized across their length as magnetically charged filaments. Positive and negative charge signs on opposite sides of the strip should form a potential barrier ridge and a potential valley groove for the positive H_z vortices, as shown in Fig. 6. For a long line with a linear charge density $\rho_l = \pm M d_f$, the magnetic field is directed radially from the line and decays as $H_s = \rho_l / 2\pi R$, with radius R about the line. This approximation is valid when the length of the line is much larger than all other dimensions in the problem. Then for a normal vortex evaluated as a point magnetic charge of $2\Phi_0$ [79], the charged strip edge will form a linear potential $U = \pm \int 2\Phi_0 H_s dx$ for vortex motion across the edge, logarithmically decaying with R. The spatial variations of the potential $U \sim \ln R$ and appropriate pinning forces $F_p \sim 1/R$ (in arbitrary units) in the gap area between the Py strips are shown in Fig. 6. Here the divergence of U and F_p at small distances is eliminated by a cutoff radius of the order of the FM film thickness. The large distance divergence of the logarithm cancels due to the opposite charges on either side of the interstrip gaps.

Accurate calculations of the strip edge-vortex coupling force with exact analytical formulas that account for the SC screening effects are discussed in the Appendix. They yield a magnetic pinning curve very close to that shown in Fig. 6 at larger distances but smoothed $F_P(R)$ close to the strip edges due to supercurrents induced by H_s. In spite of this disparity, the simple analysis based on the interactions of linear and point magnetic charges yields a clear physical

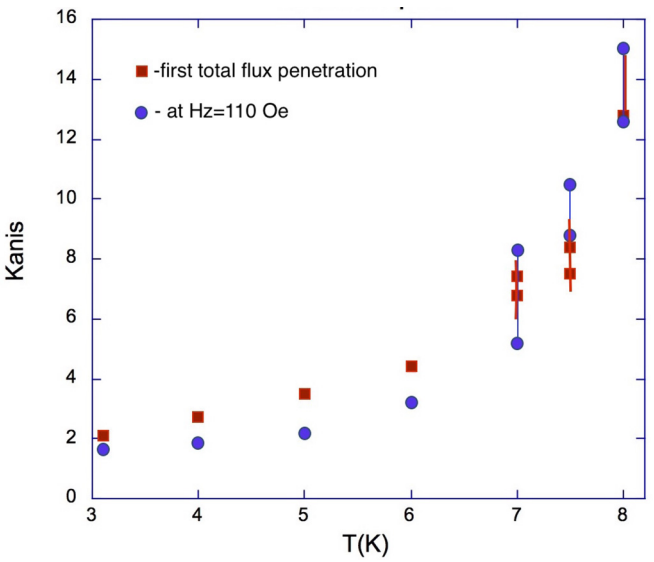

FIG. 8. Ratio of the critical currents along and across transversely polarized Py strips estimated from positions of SCT lines in MO patterns. At $T > 7$ K, estimates are approximate and presented by double dots.

interpretation. Qualitatively similar description of magnetic pinning by FM microstructures was obtained within the London approximation for individual in-plane magnetized FM bars above a SC film in Ref. [51]. However, the integral formulas in Ref. [51] are dependent on the magnet bar shape, which is different from our geometry. In our case, long edges of the transversely polarized Py strips introduce strong anisotropy to the critical currents with preferred current flow along the strip edges. Such anisotropy, responsible for the oscillating current patterns shown in Fig. 5, is clearly revealed in our experiments (Figs. 2–4).

C. Temperature variations of the vortex motion anisotropy induced by transversely polarized strips

In Fig. 7, we present the global critical state pictures observed in the sample at different temperatures. As noted above, in the areas without magnetic strips at the sample periphery, the SCT lines follow the square diagonals due to the isotropic currents in pure Nb film. In the area under the magnetic strips, the SCT lines change their direction and form an envelopelike pattern, corresponding to the critical current anisotropy. The ratio of the average currents along and across the strips, $k = J_{c\parallel}/J_{c\perp}$, depends on the applied normal field and changes with temperature. Estimates of $k(T)$ obtained from the MO patterns at smaller (squares) and larger H_z (circles) are presented in Fig. 8. At $T > 7$ K, the positions of the SCT lines in the Py pattern area are not well defined, and the values of k can be estimated only approximately. Figures 7 and 8 clearly show that the anisotropy increases with temperature. Such a behavior could be expected since at high temperatures the conventional vortex pinning by inherent defects decreases and the magnetic pinning by Py strip edges becomes the dominant factor dictating vortex motion. At $T < 7$ K, the error in the k values is small, and the plot shows that at least in this temperature range the anisotropy decreases at larger fields. This corresponds to the decreased efficiency of Py strip induced magnetic pinning upon enhancement of intervortex interactions.

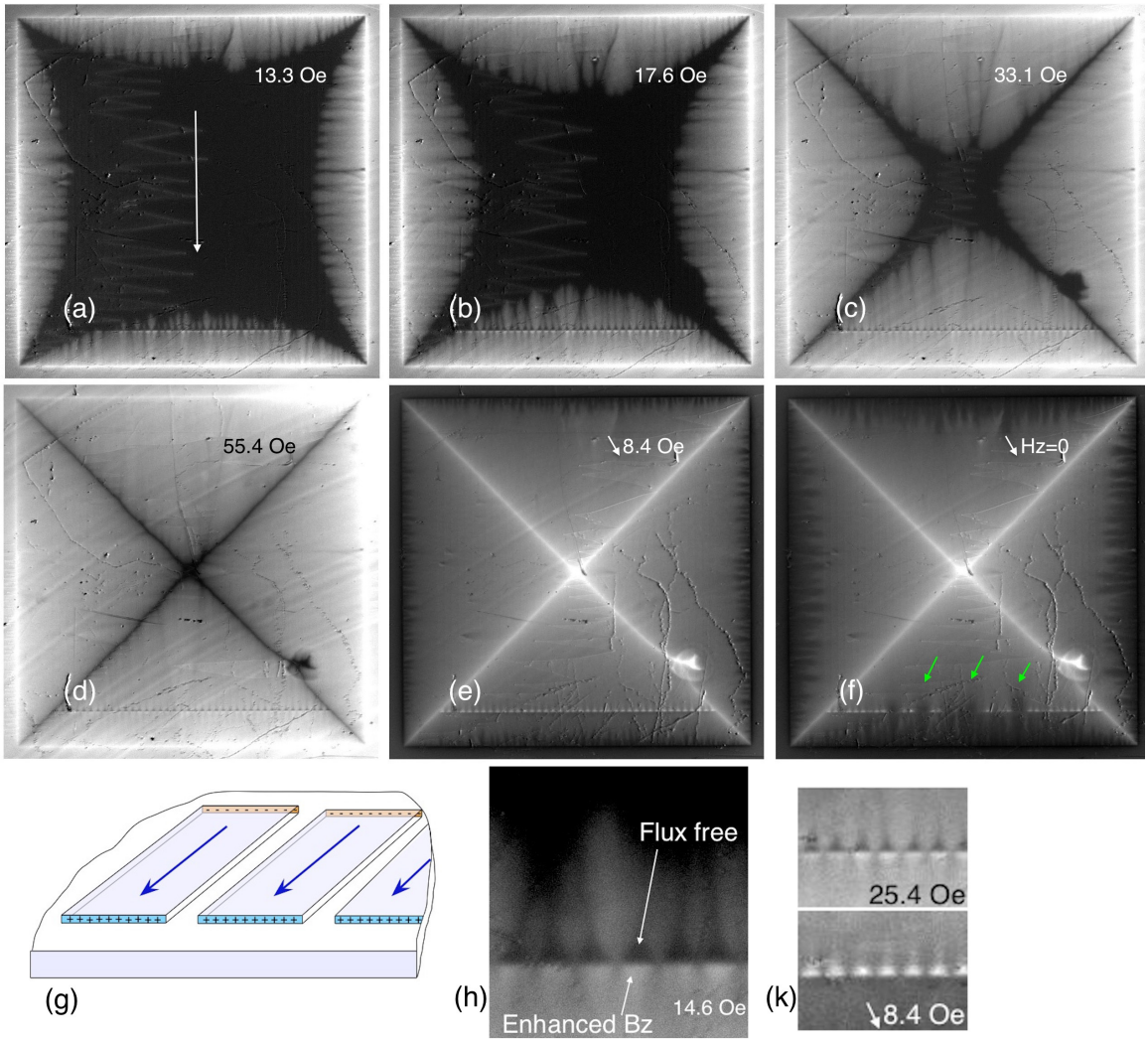

FIG. 9. Normal flux in the sample with longitudinally polarized Py strips in increasing (a)–(d) and decreasing (e) and (f) magnetic field H_z at $T = 4$ K. The direction of the in-plane field is shown in (a) by the arrow. (g) Schematic of magnetic charges emerging at short ends of the strips. (h) Expanded view of the vortex distribution near the bottom line of strip ends at smaller H_z. (k) Inversion of the flux "rhombs" near the positive strip ends with increasing (top) and decreasing H_z (bottom).

D. Longitudinal polarization of Py strips

For in-plane magnetic fields applied parallel to the strip length, the magnetic charges are localized at the narrow strip ends, as shown in Fig. 9. Small gaps between strips are neutral, although there are decaying stray fields from the neighboring strip ends. As before, we can consider the ends of the thin Py strips, which are much longer than the film thickness, as filaments of positively and negatively charged magnetic monopoles. Therefore, they should form potential barrier ridges and potential valley grooves for H_z-vortex motion. However, unlike the transverse strip polarization, which induces periodic potential lines all over the magnetic pattern, the longitudinal polarization of the strips yields only two dashed potential lines (interrupted by the interstrip gaps) at the top and bottom edges of the patterned area. The sign of the charge at the strip ends will define the vortex entry across them. Indeed, we observe accumulation of positive H_z vortices at the positively charged strip ends [dashed bright contrast near the bottom line of the strip ends in Figs. 9(a)–9(d) and in the expanded view Fig. 9(h)], and unobstructed vortex entry across the negatively charged strip ends at the top of the sample. At the bottom, the flux penetrates in the patterned area through the gaps between the positively charged ends. Here vortices enter in the shape of extended B_z balloons, and vortex-free (dark) triangular regions remain behind the strip ends [Figs. 9(b) and 9(h)]. Although the depth of B_z penetration at the top and bottom of the sample appear to be practically identical, the total amount of vortices entering across the positively charged strip ends is smaller than that passing through the negatively charged ends. This difference is more noticeable for narrower gaps between the strips [75]. On the left and right neutral sides of the Py pattern, the effect of the strips is not visible.

With further increasing H_z, the normal flux penetrates deeper from all sides [Fig. 9(c)]. However, new vortices enter without a delay across the top (negative) and left and right (uncharged) edges of the Py pattern, where they form a smooth pillow-shaped front. The only barrier remains at the positively charged bottom strip ends, where the flux enters through the interstrip gaps and then spreads under neighboring strips. Deeper into the sample, the extended vortex balloons coalesce into a smooth B_z front. New vortices accumulate near the external side of the positive strip ends, leaving the small vortex density at their inner side, as revealed by characteristic bright/dark diamonds in Figs. 8(b), 8(c), and 8(k). At larger normal fields, when B_z occupies the entire sample and forms the global critical state, the SCT lines follow the square diagonals of the sample, indicating the absence of the average current anisotropy [Fig. 9(d)]. However, the darker/brighter diamonds (although with weaker contrast) still remain along the bottom Py strip ends.

The contrast in the MO images inverts with subsequent ramp down of H_z. The exiting positive H_z vortices now accumulate at the inner side of the positively charged strip ends, leaving a smaller B_z on the outer side, hence forming the inverted diamond patterns [Figs. 9(e) and 9(k)]. Finally, at $H_z = 0$, balloons of negative vortices (dark) enter from the sample edges across the positive (bottom) ends of the Py strips without obstruction [see green arrows in Fig. 9(f)].

At $T > 6$ K, the flux patterns in both increasing and decreasing normal fields reveal an apparent interaction between the longitudinally polarized Py strips and the incoming and outgoing H_z induced vortices. Figures 10(a)–10(c) show that with increasing H_z, the flux streaks extend along the strips and follow the strip period. Minimum B_z position, separating the streaks, is settled along the middle lines of the strips. Maximum B_z forms along the interstrip gaps, indicating the preferable propagation of the positive vortices along the gaps. This occurs at both top and bottom ends of the strips, even though the dark-bright diamonds appear only at the positive (bottom) strip ends. Vortex motion across the strips at the left and right sides of the strip pattern remains basically unperturbed with a smooth B_z distribution absent of strip periodicity. With decreasing H_z, the vortices preferentially exit the sample along the interstrip gaps, leaving behind bands of reduced B_z [Figs. 10(d)–10(f)]. The observed flux periodicity indicates that at larger temperature, the coupling between the vortices and the Py strips (probably due to weak polarization of Py by the vortex field) overcomes vortex pinning by inherent defects even when the long strip edges are not magnetically charged. This coupling is also revealed by the appearance of the anisotropic envelope pattern in the global critical state. It is better seen in Figs. 10(e) and 10(f), where a short *vertical* SCT line appears at the center. It points to slightly smaller average currents *along* Py strips, corresponding to easier vortex exit across the strips towards their gaps along which they then exit to the sample edges. This anisotropy, though, is much smaller than that for the transversely polarized strips.

E. Diagonally polarized Py strips

When the in-plane magnetic field is applied along the diagonal of the Py pattern, the magnetic charges, although smaller, appear along both the long sides and short ends of the strips. Here, we observe both vortex guiding along the interstrip gaps and magnetic pinning at the positively charged strip ends (Fig. 11). However, both effects are weaker than for purely transverse and longitudinal strip polarizations, as described below.

In Fig. 12, the H_z-vortex distributions are compared for transverse, diagonal, and longitudinal polarizations of the Py pattern at the same fixed normal field and temperature of $H_z = 15.4$ Oe and $T = 4$ K, respectively. Qualitatively, the diagonally magnetized strips act very similar to the transversely polarized strips, although the penetration of B_z along the interstrip gaps [bright lines in Figs. 12(a) and 12(b)] is shallower. Also, at the bottom strip ends, there are dark/bright diamond structures, as in the case for longitudinal polarization but with weaker contrast (i.e., with smaller B_z gradient).

In Figs. 12(d)–12(f), we compare the global critical state images at 4 K for all three directions of $H_{||}$ at $H_z = 66.2$ Oe. As expected, the envelope pattern shows smaller anisotropy for diagonal Py strip polarization than for the perpendicular polarization.

The above observations show that vortex guided motion resulting from magnetic charges along the long strip edges is the major effect of the Py strip array. It produces the largest dynamic anisotropy, which can be easily tuned by changing the angle of the in-plane field with respect to the magnetic

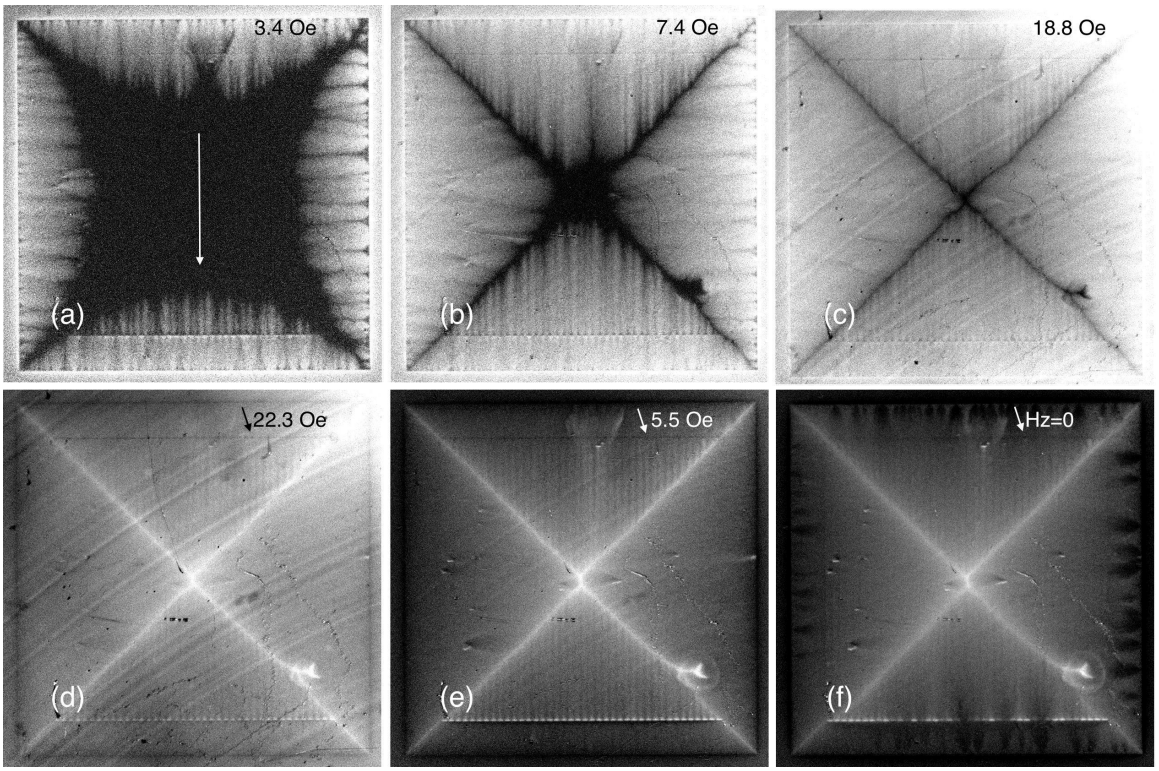

FIG. 10. Normal flux entry (a)–(c) and exit (d)–(f) in the sample with longitudinally polarized strips at 7 K. The flux streaks from the top and bottom Py pattern sides follow the strip periodicity with maximum B_z at the interstrip gaps. The flux entry across the strips (from the left and right sides of the Py pattern) lacks periodicity. The anisotropy of the exiting vortex dynamics yields short vertical SCT line in the sample center as shown in (e) and (f).

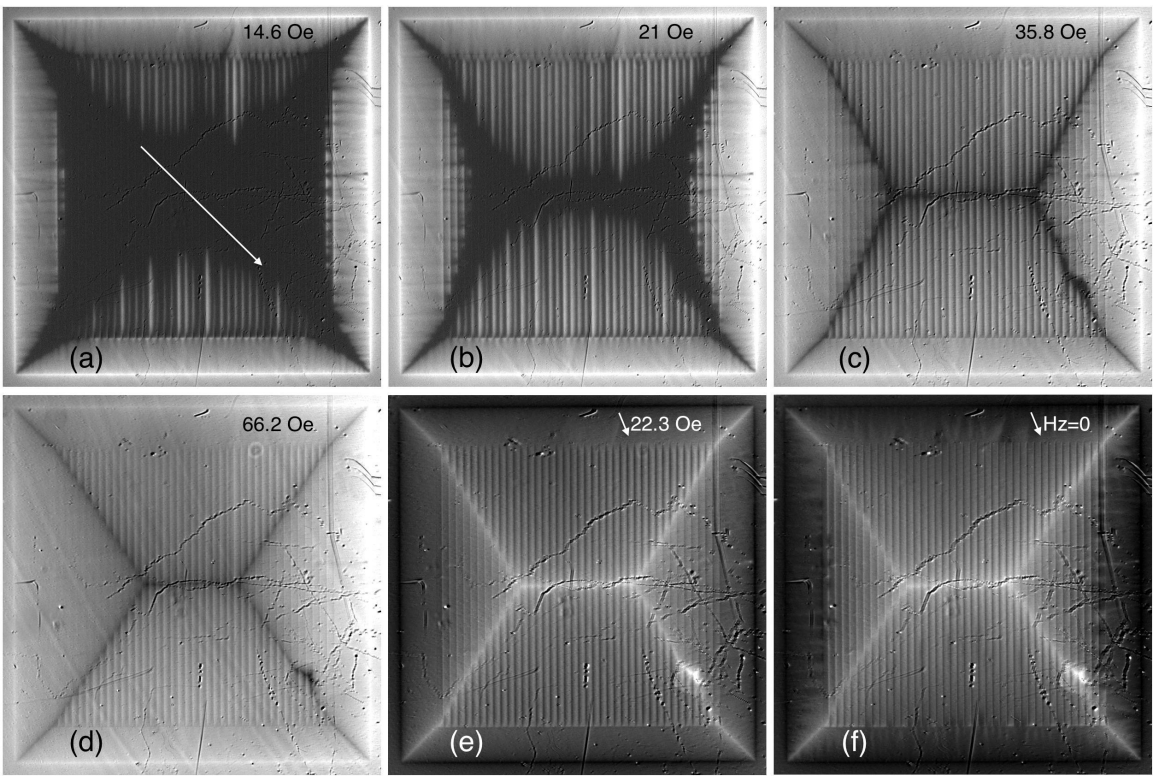

FIG. 11. Normal flux entry (a)–(d) and exit (e) and (f) in the sample with diagonally polarized strips; $T = 4$ K. The in-plane field direction is shown by an arrow in (a).

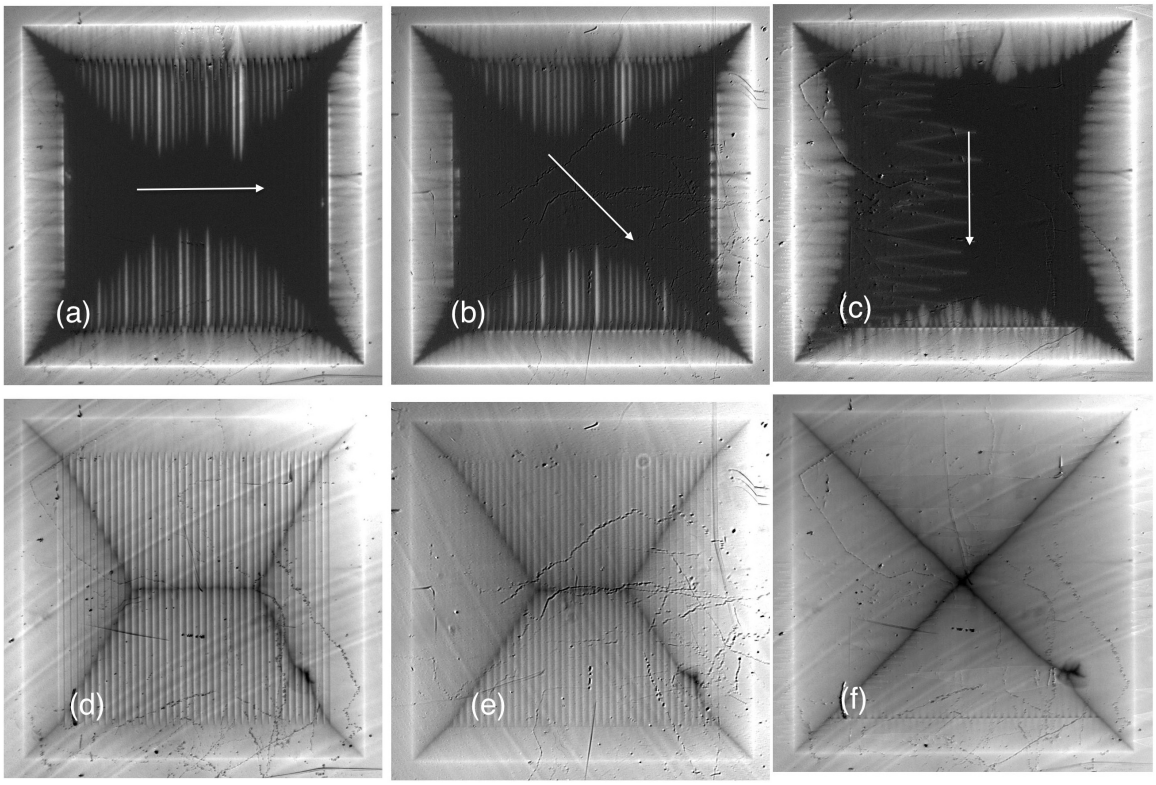

FIG. 12. Comparison of the flux distributions at the initial stage of magnetization (top row: $H_z = 15.4$ Oe) and in the total critical state (bottom row: $H_z = 66.2$ Oe) for three different polarization directions of the Py strip obtained at $T = 4$ K. Directions of the in-plane field are shown in the top pictures by white arrows.

strips. In addition, at the ends of the Py strips, it is possible to create a grid of strong pinning barriers regulating the entry of normal vortices through the interstrip gaps. The barrier effect is maximum for longitudinal strip polarization and also can be tuned by rotating the in-plane field from the long strip axis. Therefore, it is possible to manipulate the normal vortex entry in the Py patterned area in a controllable way.

III. CONCLUSIONS

A parallel array of soft FM strips with in-plane magnetization on top of a SC film allows tunable manipulation of Abrikosov vortices. Extending our earlier finding [75], in this paper we conducted a comprehensive study of the interactions between thin Py strips and vortices in a Nb film and discussed the nature of the observed vortex guiding and magnetic pinning effects.

The main action of Py strips on the underlying vortex dynamics is the control of vortex entry and exit in the sample. It arises from the magnetic charges emerging at the polarized strip edges and is defined by their magnetization component perpendicular to the edge. Abrikosov vortices interact with these linear charges as positive or negative pointlike magnetic monopoles, depending on the vortex polarity. When the strips are transversely magnetized by the in-plane field, positive and negative magnetic charges formed at opposite long edges create repulsive barrier ridge and attractive valley groove for the Abrikosov vortices. The strongly increasing magnetic potential at small distances from the lines of charged strip edges (in the first approximation as lnR) causes a substantial supercurrent anisotropy. The anisotropy is enhanced *locally* near the strip edges and results in meandering current trajectories with sharp bends at the edges. It supports advanced penetration of vortices along the strip edges of the same magnetic polarity and increased pinning for vortices moving across the edges. For vortices of the opposite magnetic polarity, the strip edges do not show a noticeable delay due to acceleration of vortices attracted towards such edges.

When the Py strips are polarized longitudinally, their ends can work as a grid, where the gaps between the strips act as gates, while the ends themselves form an efficient barrier for Abrikosov vortices. Reducing the gap width provides stronger gating effect [75]. By rotating the magnetization of the Py strips with a relatively small in-plane field, the magnetic charges at their edges can be changed, which allows tuning the effects of the strip pattern on the flux dynamics from vortex acceleration to inhibition.

We envision that by choosing appropriate material parameters (such as low pinning SC and soft FM components) and dimensions of the hybrid structure (thickness of SC and FM films, length and width of the strips, and the size of the interstrip gap), it will be possible to fabricate components for controlling individual vortex motion for flux quantum electronics.

ACKNOWLEDGMENTS

This paper was supported by the U.S. Department of Energy (DOE), Office of Science, Materials Sciences and Engineering

Division. The work of F. Colauto at Argonne National Laboratory was supported by the São Paulo Research Foundation (FAPESP) under Grant No. 2015/06.085-3. We used sample manufacturing facilities of the Center for Nanoscale Materials, supported by the U. S. DOE, Office of Science, Office of Basic Energy Sciences, under Contract No. DE-AC02-06CH11357. A. I. Buzdin acknowledges support from the French National Research Agency (ANR) project "SUPERTRONICS."

APPENDIX

Here we calculate the current in the SC film (in the XY plane) induced by the edge of a long FM strip ($\|Y$), where magnetization is directed perpendicular to the edge face ($\mathbf{M}||X$). This current multiplied by the flux quantum gives the Lorentz force acting on the Abrikosov vortex from the strip edge. The force is repulsive (positive) for the same sign of the magnetic charge of the vortex and the edge and attractive (negative) for opposite magnetic charges. When the FM film thickness is much smaller than all other dimensions in the problem, the magnetic field can be presented as a field of a linear monopole (long thin charged filament $\|Y$). It is directed radially perpendicular to the filament and decays with radius r as $B = b/r$. The magnetic charge per unit length in this case is $b = 2Md_f$, where M is the saturation magnetization and d_f is the FM film thickness. The vector potential of the filament is $A_y = b\varphi$, where φ is azimuthal angle around the filament axis. One can check that

$$\mathrm{rot}\vec{A} = \hat{r}\left(\frac{1}{r}\frac{\partial A_y}{\partial \varphi}\right) + \hat{\varphi}\left(-\frac{\partial A_y}{\partial r}\right) = \hat{r}\frac{b}{r}\,.$$

Below we use the Pearl's approximation for thin SC films ($d < \lambda$), admitting a two-dimensional distribution of sheet currents, $\vec{j}_s$, in the SC film. Then

$$\mathrm{rot}\vec{B} = \frac{4\pi}{c}\vec{j}_s = -\frac{\vec{A}}{\lambda^2}\,d\delta(z).$$

The total vector potential and the magnetic field can be divided into components due to the magnetic monopole of the vortex ($\vec{A}_V, \vec{B}_V$) and due to currents induced by the magnetic filament ($\vec{A}_s, \vec{B}_s$):

$$\vec{A} = \vec{A}_V + \vec{A}_s \quad \text{and} \quad \vec{B} = \vec{B}_V + \vec{B}_s.$$

Then

$$\mathrm{rot}\vec{B} = \frac{4\pi}{c}\vec{j}_s = -\frac{\vec{A}}{\lambda^2}\,d\delta(z), \mathrm{rot}\vec{B}_V = 0 \rightarrow \mathrm{rot}\vec{B}_s$$
$$= -\frac{\vec{A}}{\lambda^2}\,d\delta(z) = \frac{-d}{\lambda^2}[\vec{A}_V(z=0) + \vec{A}_s(z=0)]$$

$\mathrm{rot}\vec{B}_s = -\nabla^2\vec{A}_s$, and after Fourier transformation:

$$-(q^2+k^2)A_s(q,k) = [A_M(q,z=0) + A_s(q,z=0)]\frac{1}{\lambda_{\mathrm{eff}}}$$

with $\lambda_{\mathrm{eff}} = \frac{\lambda^2}{d}$, $q = (q_x, q_y)$, and $k = k_z$.

Then skipping the index $z = 0$, we write the relation for $A_M(q)$ and $A_s(q)$ as

$$A_s(q) = \int A_s(q,k)\frac{dk}{2\pi} = -\frac{A_M + A_s}{2\pi\lambda_{\mathrm{eff}}}\int\frac{dk}{q^2+k^2}$$
$$= -\frac{A_M + A_s}{2\lambda_{\mathrm{eff}}q},$$

so that $A_s(q) = \frac{-A_M(q)}{1+2\lambda_{\mathrm{eff}}q}$.

Then current in the SC film is

$$\vec{j}(q) = -\frac{c}{4\pi\lambda_{\mathrm{eff}}}(\vec{A}_M + \vec{A}_s) = -\frac{c}{4\pi\lambda_{\mathrm{eff}}}\frac{2\lambda_{\mathrm{eff}}q}{1+2\lambda_{\mathrm{eff}}q}\vec{A}_M$$
$$= -\frac{c}{2\pi}\frac{q}{1+2\lambda_{\mathrm{eff}}q}\vec{A}_M.$$

Now we consider the gap between two magnetic strips, where the fields are produced by two oppositely charged filaments at a distance w and at some height h above the superconductor ($h \sim d_f/2$). Using the azimuthal angle $\varphi = \mathrm{arctg}(x/h)$, the total vector potential A_M is

$$A_y(x) = b\left[\mathrm{arctg}\left(\frac{x}{h}\right) - \mathrm{arctg}\left(\frac{x+w}{h}\right)\right].$$

Accounting for the fact that h is small, we replace arctg with a step function of height π so that the Fourier transform of $A_y(x)$ becomes

$$A_q^y = \pi b\int_0^W e^{iqx}dx = -\frac{\pi b}{iq}(1 - e^{iqw}).$$

Then the current distribution can be calculated as inverse Fourier Transform by substituting A_q^y in the above formula for J_q,

$$J(x) = \frac{1}{2\pi}\int_{-\infty}^{\infty}J_q e^{-iqx}dq = \frac{1}{2\pi}\int_0^{\infty}(J_q e^{-iqx} + J_{-q}e^{iqx})dq$$
$$= \frac{b}{2}\frac{c}{2\pi}\int_0^{\infty}\frac{-i}{1+2q\lambda_{\mathrm{eff}}}\{(1-e^{-iqW})e^{-iqx} - (1-e^{+iqW})$$
$$\times e^{+iqx}\}dq = \frac{cb}{2\pi}\int_0^{\infty}\frac{\sin q(x+w) - \sin qx}{1+2q\lambda_{\mathrm{eff}}}dq$$

which after substitution, $2q\lambda_{\mathrm{eff}} = \tilde{q}$, $\frac{x}{2\lambda_{\mathrm{eff}}} = \tilde{x}$, $\frac{W}{2\lambda_{\mathrm{eff}}} = \tilde{W}$, becomes

$$J(x) = \frac{cb}{4\pi\lambda_{\mathrm{eff}}}\int_0^{\infty}\frac{\sin\tilde{q}(\tilde{x}+\tilde{w}) - \sin\tilde{q}\tilde{x}}{1+\tilde{q}}d\tilde{q}$$

We define function $f(x) = \int_0^{\infty}\frac{\sin qx}{1+q}dq = Ci(x)\sin x - Si(x)\cos x + \frac{\pi}{2}\cos x$, where $Ci(x) = -\int_x^{\infty}\frac{\cos t}{t}dt$ is the cosine integral and $Si(x) = \int_0^x\frac{\sin t}{t}dt$ is the sine integral. Then, $J(x) = \frac{cb}{4\pi\lambda_{\mathrm{eff}}}[f(x+w) - f(x)]$.

Asymptotically, the cosine integral shows the logarithmic behavior for small arguments and saturates at large x:

$Ci(x \rightarrow 0) \rightarrow \gamma + \ln x$ ($\gamma = 0.5772$ is the Euler constant), while $Ci(x \rightarrow \infty) \rightarrow 0$.

The sine integral at small x tends to zero $Si(x \rightarrow 0) \rightarrow 0$, and $Si(x \rightarrow \pm\infty) \rightarrow \pm\pi/2$.

However, one has to carefully choose the branches of $Ci(x)$ and $Si(x)$ for the intermediate x, which otherwise can result in a strongly oscillating function.

[1] H. Toepfer and T. Ortlepp, Design infrastructure for rapid single flux quantum circuits, Cryogenics **49**, 643 (2009).

[2] S. Anders, M. G. Blamire, F.-Im. Buchholz, D.-G. Crété, R. Cristiano, P. Febvre, L. Fritzsch, A. Herr, E. Il'ichev, J. Kohlmann, J. Kunert , H.-G. Meyer, J. Niemeyer, T. Ortlepp, H. Rogalla, T. Schurig, M. Siegel, R. Stolz, E. Tarte, H. J. M. ter Brake, H. Toepfer, J.-C. Villegier, A. M. Zagoskin, and A. B. Zorin, European roadmap on superconductive electronics—status and perspectives, Physica C **470**, 2079 (2010).

[3] O. A. Mukhanov, Energy-efficient single flux quantum technology, IEEE Trans. Appl. Supercond. **21**, 760 (2011).

[4] K. K. Likharev, Superconductor digital electronics, Physica C **482**, 6 (2012).

[5] J. Kunert, O. Brandel, S. Linzen, O. Wetzstein, H. Toepfer, T. Ortlepp, and H.-G. Meyer, Recent developments in superconductor digital electronics technology at FLUXONICS Foundry, IEEE Trans. Appl. Supercond. **23**, 1101707 (2013).

[6] D. S. Holmes, A. L. Ripple, and M. A. Manheimer, Energy-efficient superconducting computing—power budgets and requirements, IEEE Trans. Appl. Supercond. **23**, 1701610 (2013).

[7] T. Golod, A. Iovan, and V. M. Krasnov, Single Abrikosov vortices as quantized information bits, Nat. Commun. **6**, 8628 (2015).

[8] A. A. Abrikosov, On the magnetic properties of superconductors of the second group, Sov. Phys. JETP **5**, 1174 (1957) [Zh. Exp. Teor. Fiz. **32**, 1442 (1957)].

[9] A. F. Hebard and A. T. Fiory, A memory device utilizing the storage of Abrikosov vortices at an array of pinning sites in a superconducting film, AIP Conf. Proc. **44**, 465 (1978).

[10] W. Bachtold, The vortex file: A proposal for a new application of type-II superconductivity, IEEE Trans. Magn. **15**, 558 (1979).

[11] S. Uehara and K. Nagata, Trapped vortex memory cells, Appl. Phys. Lett. **39**, 992 (1981).

[12] J. Parisi, R. P. Huebener, and B. Mühlemeier, Experimental study of a superconducting vortex-memory device, Appl. Phys. Lett. **40**, 907 (1982).

[13] J. Parisi and R. P. Huebener, A superconducting vortex-memory system, IEEE Trans. Electron. Devices **31**, 310 (1984).

[14] K. Miyahara, M. Mukaida, and K. Hohkawa, Abrikosov vortex memory, Appl. Phys. Lett. **47**, 754 (1985); Abrikosov vortex memory with improved sensitivity and reduced write current levels, IEEE Trans. Magn. **23**, 875 (1987).

[15] J. F. Wambaugh, C. Reichhardt, C. J. Olson, F. Marchesoni, and F. Nori, Superconducting Fluxon Pumps and Lenses, Phys. Rev. Lett. **83**, 5106 (1999).

[16] M. B. Hastings, C. J. Olson Reichhardt, and C. Reichhardt, Ratchet Cellular Automata, Phys. Rev. Lett. **90**, 247004 (2003).

[17] B. Y. Zhu, F. Marchesoni, V. V. Moshchalkov, and F. Nori, Controllable step motors and rectifiers of magnetic flux quanta using periodic arrays of asymmetric pinning defects, Phys. Rev. B **68**, 014514 (2003).

[18] J. E. Villegas, S. Savel'ev, F. Nori, E. M. Gonzalez, J. V. Anguita, R. Garcia, and J. L. Vicent, A superconducting reversible rectifier that controls the motion of magnetic flux quanta, Science **302**, 1188 (2003).

[19] M. Berciu, T. G. Rappoport, and B. Janko, Manipulating spin and charge in magnetic semiconductors using superconducting vortices, Nature **435**, 71 (2005).

[20] S. Ooi, S. Savel'ev, M. B. Gaifullin, T. Mochiku, K. Hirata, and F. Nori, Nonlinear Nanodevices Using Magnetic Flux Quanta, Phys. Rev. Lett. **99**, 207003 (2007).

[21] M. Milosevic, G. R. Berdiyorov, and F. M. Peeters, Fluxonic cellular automata, Appl. Phys. Lett. **91**, 212501 (2007).

[22] K. Yu, T. W. Heitmann, C. Song, M. P. DeFeo, B. L. T. Plourde, M. B. S. Hesselberth, and P. H. Kes, Asymmetric weak-pinning superconducting channels: Vortex ratchets, Phys. Rev. B **76**, 220507 (2007).

[23] W. Gillijns, A. V. Silhanek, V. V. Moshchalkov, C. J. O. Reichhardt, and C. Reichhardt, Origin of Reversed Vortex Ratchet Motion, Phys. Rev. Lett. **99**, 247002 (2007).

[24] N. Verellen, A. V. Silhanek, W. Gillijns, V. V. Moshchalkov, V. Metlushko, F. Gozzini, and B. Ilic, Switchable magnetic dipole induced guided vortex motion, Appl. Phys. Lett. **93**, 022507 (2008).

[25] A. Yu. Aladyshkin, J. V. de Vondel, C. C. D. Silva, and V. V. Moshchalkov, Tunable anisotropic nonlinearity in superconductors with asymmetric antidot array, Appl. Phys. Lett. **93**, 082501 (2008).

[26] R. Woerdenweber, E. Hollmann, J. Schubert, R. Kutzner, and A. K. Ghosh, Pattern induced phase transition of vortex motion in high-T-c films, Appl. Phys. Lett. **94**, 202501 (2009).

[27] J. F. He, N. Harada, T. Ishibashi, H. Naitou, and H. Asada, Magneto-optical observation of anisotropic critical current density in Nb films with artificial asymmetric pinning potential, Jap. J. Appl. Phys. **48**, 063003 (2009).

[28] B. B. Jin, B. Y. Zhu, R. Wördenweber, C. C. de Souza Silva, P. H. Wu, and V. V. Moshchalkov, High-frequency vortex ratchet effect in a superconducting film with a nanoengineered array of asymmetric pinning sites, Phys. Rev. B **81**, 174505 (2010).

[29] A. V. Kapra, V. R. Misko, D. Y. Vodolazov, and F. M. Peeters, The guidance of vortex-antivortex pairs by in-plane magnetic dipoles in a superconducting finite-size film, SUST **24**, 024014 (2011).

[30] A. V. Kapra, V. R. Misko, and F. M. Peeters, Controlling magnetic flux motion by arrays of zigzag-arranged magnetic bars, SUST **26**, 025011 (2013).

[31] J. Trastoy, C. Ulysse, R. Bernard, M. Malnou, N. Bergeal, J. Lesueur, J. Briatico, and J. E. Villegas, Tunable Flux-Matching Effects in High-Tc Superconductors with Nonuniform Pinning Arrays, Phys. Rev. Appl. **4**, 054003 (2015).

[32] J. del Valle, A. Gomez, E. M. Gonzalez, M. R. Osorio, D. Granados, and J. L. Vicent, Superconducting/magnetic three-state nanodevice for memory and reading applications, Sci. Rep. **5**, 15210 (2015).

[33] O. V. Dobrovolskiy, M. Huth, and V. A. Shklovskij, Alternating current-driven microwave loss modulation in a fluxonic metamaterial, Appl. Phys. Lett. **107**, 162603 (2015).

[34] V. V. Moshchalkov and J. Fritzsche, *Nanostructured Superconductors* (World Scientific, Singapore, 2011).

[35] A. Yu. Aladyshkin, A. I. Buzdin, A. A. Fraerman, A. S. Mel'nikov, D. A. Ryzhov, and A. V. Sokolov, Domain-wall superconductivity in hybrid superconductor-ferromagnet structures, Phys. Rev. B **68**, 184508 (2003).

[36] Z. R. Yang, M. Lange, A. Volodin, R. Szymczak, and V. V. Moshchalkov, Domain-wall superconductivity in superconductor-ferromagnet hybrids, Nat. Mater. **3**, 793 (2004).

[37] A. V. Silhanek, V. N. Gladilin, J. Van de Vondel, B. Raes, G. W. Ataklti, W. Gillijns, J. Tempere, J. T. Devreese, and V. V.

Moshchalkov, Local probing of the vortex–antivortex dynamics in superconductor/ferromagnet hybrid structures, SUST **24**, 024007 (2011).
[38] O. Geoffroi, D. Givord, Y. Otani, B. Pannetier, and F. Ossart, Magnetic and transport properties of ferromagnetic particulate arrays fabricated on superconducting thin-films, J. Magn. Magn. Mater. **121**, 223 (1993).
[39] Y. Otani, B. Pannetier, J. P. Nozieres, and D. Givord, Magnetostatic interactions between magnetic arrays and superconducting thin-films, J. Magn. Magn. Mater. **126**, 622 (1993).
[40] V. V. Metlushko, M. Baert, R. Jonckheere, V. V. Moshchalkov, and Y. Bruynseraede, Matching effects in Pb/Ge multilayers with the lattice of submicron holes, Sol. St. Commun. **91**, 331 (1994).
[41] M. Baert, V. V. Metlushko, R. Jonckheere, V. V. Moshchalkov, and Y. Bruynseraede, Composite Flux-Line Lattices Stabilized in Superconducting Films by a Regular Array of Artificial Defects, Phys. Rev. Lett. **74**, 3269 (1995).
[42] J. I. Martin, M. Velez, J. Nogues, and I. K. Schuller, Flux Pinning in a Superconductor by an Array of Submicrometer Magnetic Dots, Phys. Rev. Lett. **79**, 1929 (1997).
[43] Y. Jaccard, J. I. Martin, M. C. Cyrille, M. Velez, J. L. Vicent, and I. K. Schuller, Magnetic pinning of the vertex lattice by arrays of submicrometric dots, Phys. Rev. B **58**, 8232 (1998).
[44] J. L. Martin, M. Velez, A. Hoffmann, I. K. Schuller, and J. L. Vicent, Artificially Induced Reconfiguration of the Vortex Lattice by Arrays of Magnetic Dots, Phys. Rev. Lett. **83**, 1022 (1999).
[45] I. F. Lyuksyutov and V. L. Pokrovsky, Magnetization Controlled Superconductivity in a Film with Magnetic Dots, Phys. Rev. Lett. **81**, 2344 (1998).
[46] I. F. Lyuksyutov and D. G. Naugle, Frozen flux superconductors, Mod. Phys. Lett. B **13**, 491 (1999).
[47] S. Erdin, A. F. Kayali, I. F. Lyuksyutov, and V. L. Pokrovsky, Interaction of mesoscopic magnetic textures with superconductors, Phys. Rev. B **66**, 014414 (2002).
[48] I. K. Marmorkos, A. Matulis, and F. M. Peeters, Vortex structure around a magnetic dot in planar superconductors, Phys. Rev. B **53**, 2677 (1996).
[49] M. V. Milosevic, S. V. Yampolskii, and F. M. Peeters, Magnetic pinning of vortices in a superconducting film: The (anti)vortex-magnetic dipole interaction energy in the London approximation, Phys. Rev. B **66**, 174519 (2002).
[50] M. V. Milosevic and F. M. Peeters, Interaction between a superconducting vortex and an out-of-plane magnetized ferromagnetic disk: Influence of the magnet geometry, Phys. Rev. B **68**, 094510 (2003).
[51] M. V. Milosevic and F. M. Peeters, Vortex pinning in a superconducting film due to in-plane magnetized ferromagnets of different shapes: The London approximation, Phys. Rev. B **69**, 104522 (2004).
[52] M. V. Milosevic and F. M. Peeters, Vortex-antivortex nucleation in superconducting films with arrays of in-plane dipoles, Physica C **437–438**, 208 (2006).
[53] C. J. Olson, C. Reichhardt, B. Janko, and F. Nori, Collective Interaction-Driven Ratchet for Transporting Flux Quanta, Phys. Rev. Lett. **87**, 177002 (2001).
[54] V. R. Misko, D. Bothner, M. Kemmler, R. Kleiner, D. Koelle, F. M. Peeters, and F. Nori, Enhancing the critical current in quasiperiodic pinning arrays below and above the matching magnetic flux, Phys. Rev. B **82**, 184512 (2010).
[55] V. R. Misko and F. Nori, Magnetic flux pinning in superconductors with hyperbolic-tesselation arrays of pinning sites, Phys. Rev. B **85**, 184506 (2012).
[56] C. C. de Souza Silva and G. Carneiro, Simple model for dynamical melting of moving vortex lattices interacting with periodic pinning, Phys. Rev. B **66**, 054514 (2002).
[57] C. C. de Souza Silva and G. Carneiro, Transverse pinning and vortex displacement fluctuations of moving vortex lattices interacting with periodic pinning, Physica C **391**, 203 (2003).
[58] G. Carneiro, Pinning and creation of vortices in superconducting films by a magnetic dipole, Phys. Rev. B **69**, 214504 (2004).
[59] G. Carneiro, Interaction between vortices in superconducting films and magnetic dipole arrays, Physica C **404**, 78 (2004).
[60] G. Carneiro, Tunable interactions between vortices and a magnetic dipole, Phys. Rev. B **72**, 144514 (2005).
[61] G. Carneiro, Tunable ratchet effects for vortices pinned by periodic magnetic dipole arrays, Physica C **432**, 206 (2005).
[62] I. F. Lyuksyutov and V. L. Pokrovsky, Ferromagnet/superconductor hybrids, Adv. Phys. **54**, 67 (2005).
[63] M. Velez, J. I. Martin, J. E. Villegas, A. Hoffman, E. M. González, J. L. Vicent, and I. K. Schuller, Superconducting vortex pinning with artificial magnetic nanostructures, J. Magn. Magn. Mater. **320**, 2547 (2008).
[64] A. Yu. Aladyshkin, A. V. Silhanek, W. Gillijns, and V. V. Moshchalkov, Nucleation of superconductivity and vortex matter in superconductor/ferromagnet hybrids, Supercond. Sci. Technol. **22**, 053001 (2009).
[65] J. Brisbois, M. Motta, J. I. Avila, G. Shaw, T. Devillers, N. M. Dempsey, S. K. P. Veerapandian, P. Colson, B. Vanderheyden, P. Vanderbemden, W. A. Ortiz, N. D. Nguyen, R. B. G. Kramer, and A. V. Silhanek, Imprinting superconducting vortex footsteps in a magnetic layer, Sci. Rep. **6**, 27159 (2016).
[66] C. Reichhardt and C. J. Olson Reichhardt, Transverse ac-driven and geometric ratchet effects for vortices in conformal crystal pinning arrays, Phys. Rev. B **93**, 064508 (2016).
[67] M. Trezza, C. Cirillo, A. L. Dolgiy, S. V. Redko, V. P. Bondarenko, A. V. Andreyenka, A. L. Danilyuk, S. L. Prischepa, and C. Attanasio, Change of the topology of a superconducting thin film electromagnetically coupled with an array of ferromagnetic nanowires, Supercond. Sci. Technol. **29**, 015011 (2016).
[68] O. V. Dobrovolskiy, Abrikosov fluxonics in washboard nanolandscapes, Physica C **533**, 80 (2016).
[69] Z. Adamus, M. Cieplak, M. Konczykowski, L. Y. Zhu, and C. L. Chien, Influence of magnetic domain landscape on the flux dynamics in superconductor/ferromagnet bilayers, Phys. Rev. B **93**, 054509 (2016).
[70] V. Vlasko-Vlasov, U. Welp, G. Karapetrov, V. Novosad, D. Rosenmann, M. Iavarone, A. Belkin, and W.-K. Kwok, Guiding superconducting vortices with magnetic domain walls, Phys. Rev. B **77**, 134518 (2008).
[71] V. K. Vlasko-Vlasov, U. Welp, A. Imre, D. Rosenmann, J. Pearson, and W.-K. Kwok, Soft magnetic lithography and giant magnetoresistance in superconducting/ferromagnetic hybrids, Phys. Rev B **78**, 214511 (2008).

[72] V. Vlasko-Vlasov, U. Welp, W. Kwok, D. Rosenmann, H. Claus, A. I. Buzdin, and A. Melnikov, Coupled domain structures in superconductor/ferromagnet Nb-Fe/garnet bilayers, Phys. Rev. B **82**, 100502 (2010).

[73] V. Vlasko-Vlasov, A. Buzdin, A. Melnikov, U. Welp, D. Rosenmann, L. Uspenskaya, V. Fratello, and W. Kwok, Domain structure and magnetic pinning in ferromagnetic/superconducting hybrids, Phys. Rev. B **85**, 064505 (2012).

[74] V. K. Vlasko-Vlasov, E. Palacios, D. Rosenmann, J. Pearson, Y. Jia, Y. L. Wang, U. Welp, and W.-K. Kwok, Self-healing patterns in ferromagnetic-superconducting hybrids, Supercond. Sci. Technol. **28**, 035006 (2015).

[75] V. K. Vlasko-Vlasov, F. Colauto, T. Benseman, D. Rosenmann, and W.-K. Kwok, Triode for magnetic flux quanta, Sci. Rep. **6**, 36847 (2016).

[76] V. K. Vlasko-Vlasov, G. W. Crabtree, U. Welp, and V. I. Nikitenko, Magneto-optical studies of magnetization processes in high-Tc superconductors, NATO ASI Ser., Ser. E **356**, 205 (1999).

[77] V. K. Vlasko-Vlasov, F. Colauto, A. I. Buzdin, D. Carmo, A. M. H. Andrade, A. A. M. Oliveira, W. A. Ortiz, D. Rosenmann, and W.-K. Kwok, Crossing fields in thin films of isotropic superconductors, Phys. Rev. B **94**, 184502 (2016).

[78] A point charge in vacuum generates fields in the 4π spatial angle. However, the effective charge of the vortex at the SC surface produces the field only in half-space outside the SC. Therefore, the vortex monopole charge appears as $2\Phi_0$.

[79] G. Carneiro and E. H. Brandt, Vortex lines in films: Fields and interactions, Phys. Rev. B **61**, 6370 (2000).

[80] V. K. Vlasko-Vlasov, U. Welp, V. Metlushko, and G. W. Crabtree, Experimental test of the self-organized criticality of vortices in superconductors, Phys. Rev. B **69**, 140504(R) (2004).

[81] M. Friesen and A. Gurevich, Nonlinear current flow in superconductors with restricted geometries, Phys. Rev. B **63**, 064521 (2001).

[82] The qualitative current patterns in Figs. 5(a) and 5(b) are constructed using the following assumptions relevant for the SC plates and films in perpendicular fields. On average, the supercurrents flow along the sample edge, and their direction corresponds to the partial screening of the increasing H_z. Distances between the current lines represent the inverse current density. The local enhancement (decrease) of B_z corresponds to the convex (concave) bending of the current lines, and the smaller bending radius yields stronger enhancement (decrease) of B_z. Within these assumptions the current patterns reproduce peculiarities of the B_z images.